



Surface radiation characteristics and downward cloud radiative forcing in southern Xinjiang during summer 2019

Jianrong Bi^{1,2,3} · Dapeng Zuo^{1,3} · Fan Yang^{1,4} · Linhan Zhang^{1,3} · Zhongwei Huang^{1,2,3} · Tianhe Wang^{1,3}

Received: 15 September 2021 / Accepted: 4 November 2021 / Published online: 25 November 2021
© The Author(s), under exclusive licence to Springer-Verlag GmbH Austria, part of Springer Nature 2021

Abstract

This study analyzed the surface radiation characteristics and evaluated downward cloud radiative forcing (CRF) in southern Xinjiang during summer 2019. Surface radiation fluxes show prominent day-to-day and diurnal variations, with the maximums of 915.6, 921.2, and 121.9 Wm^{-2} , respectively, for total, direct, and diffuse shortwave radiations under cloudless conditions. Cloud layer or dust layer could significantly impede the incident solar irradiance and moderately reduce the emission of longwave radiation to space, and hence bring a strong downward negative radiative impact. A rigorous four-step screening algorithm was applied to effectively identify the clear-sky periods based on 1-min total and diffuse shortwave irradiances. The clear-sky shortwave (SW) radiation is empirically fitted using a power law equation and cosine of solar zenith angle, and the clear-sky longwave (LW) radiation is calculated via the average diurnal cycles of all datasets of detected 1-min LW radiation under cloudless conditions. The 24-h daily mean CRFs of SW are largely negative (-204.1 to -3.3 Wm^{-2}), and corresponding LW are moderately positive (-1.5 to $+70.4 \text{ Wm}^{-2}$), which coincide with the overcast conditions or large cloud cover amounts. The overall averages of SW and LW CRFs and net cloud effect are -69.7 ± 62.3 , $+29.5 \pm 22.2$, and $-40.1 \pm 42.1 \text{ Wm}^{-2}$, respectively, implying that clouds have a net cooling effect on the regional climate. Our results are consistent with the summer mean values in northern China, but less than those in southern China, and greater than those of the global mean values. Such negative cloud radiative forcing would partly counteract the global warming induced by greenhouse gases and modulate the Earth's radiation budget balance.

1 Introduction

Solar radiation flux is the major energy source of the Earth-atmosphere system, which governs the surface temperature and drives the general atmospheric circulation and life activities on earth (Dutton et al. 2006; Shi et al. 2008;

Wild 2009). An accurate measurement of terrestrial solar irradiance is an essential basis for exploring the evolution of weather and climate change and validating the satellite retrievals (Che et al. 2005; Pinker et al. 2005; Bi et al. 2013). Clouds generally cover approximately 70% of the global surface area, and could significantly regulate the Earth's radiation budget balance through directly reflecting and scattering solar shortwave radiation and absorbing and emitting terrestrial longwave radiation (Liou 1992; Xiang et al. 2014; Li et al. 2018; Zhang et al. 2017). Detailed information of cloud microphysical (cloud phase, cloud optical thickness, condensed water path, and droplet effective radius) and macrophysical (cloud amount, cloud height, and cloud frequency) properties are vital to accurately assess its climatic impacts (Li et al. 2009; McFarlane et al. 2013; Zhang et al. 2013). The Intergovernmental Panel on Climate Change (Boucher et al. 2013) indicated that cloud radiative feedbacks in climate models currently remained great uncertainties due to lack of comprehensive knowledge of vertical structure and key parameters of the cloud. Hence, a reasonable evaluation and understanding of cloud radiative forcing is of prime

Responsible Editor: Xinxin Xie.

✉ Jianrong Bi
bjjr@lzu.edu.cn

- ¹ Key Laboratory for Semi-Arid Climate Change of the Ministry of Education, College of Atmospheric Sciences, Lanzhou University, Lanzhou 730000, China
- ² Collaborative Innovation Center for Western Ecological Safety, Lanzhou University, Lanzhou 730000, China
- ³ Gansu Provincial Field Scientific Observation and Research Station of Semi-Arid Climate and Environment, Lanzhou 730000, China
- ⁴ Taklimakan Desert Meteorology Field Experiment Station, Institute of Desert Meteorology, China Meteorological Administration (CMA), Urumqi 830002, China

importance to accurately predict cloud feedbacks in the future climate and hydrological cycle.

The Taklimakan Desert in northwest China is located in the center of the Tarim Basin and is believed to be the second largest shifting sand-dune desert in the world, and covers approximately $3.376 \times 10^5 \text{ km}^2$ (Wang et al. 2017), with the east–west-oriented of 1000 km and south–north-oriented of 400 km. The Tarim Basin is surrounded by magnificent mountains, with the Kunlun Mountains (elevation of 5500–6000 m) to the south, the Pamirs (elevation of 4500–7500 m) to the west, and the Tianshan Mountain (elevation of 4000–7400 m) to the north, and the east is spread over the Great Gobi and Kumtag Desert. There are abundant sun light resources, sparse vegetation, and drastic temperature difference between daytime and nighttime in the Tarim Basin. On account of its unique topographic and environmental conditions, the climate of the region is characterized by little precipitation, strong evaporation, deep boundary layer structure during daytime, and frequent dust storm (Wang et al. 2016; Yang et al. 2021). He et al. (2008) analyzed the terrestrial solar radiation features and its influencing factors in Taklimakan Desert hinterland (Tazhong station) and indicated that global shortwave radiation was very strong in summer, with an instantaneous maximum of 1182.6 Wm^{-2} , and the total cloud cover and mineral dust were two primary contributors for intensely reducing the surface solar radiation. Nevertheless, the occurrences of cloud and dust storms exerted relatively small effects on terrestrial longwave radiation in Tazhong, which could increase slightly the surface longwave radiation (Li et al. 2012). Chen et al. (2009) displayed that the total cloud cover in Taklimakan Desert reached the maximum value of 50% in July, and the minimum value was only 12% in October, using the CERES SSF Aqua MODIS Edition 1B datasets from 2002 to 2004. Based on FY-2F satellite products, Li et al. (2019) investigated the cloud characteristics in Xinjiang region, and showed that the annual average of total cloud fraction in Xinjiang was about 37.7%, while the mean total cloud cover in Tarim Basin was the lowest ($\sim 26.1\%$), of which was much more in daytime than that in nighttime. Cloud radiative forcing (CRF) is an important quantity to examine the cloud feedbacks (heating or cooling effect) on the regional climate (Ramanathan et al. 1989; Mace et al. 2006). And Li et al. (2017) demonstrated that CRFs over the arid zones of the Northern Hemisphere were closely related to the cloud fraction. Huang et al. (2006) investigated the possible influences of dust aerosols on cloud properties and RF over northwestern China using data collected MODIS and CERES instruments, and suggested that the instantaneous net CRFs of pure clouds and dust-contaminated clouds are -161.6 Wm^{-2} and -118.6 Wm^{-2} , respectively. Su et al. (2008) extended the study of Huang et al. (2006) using the Fu-Liou radiative model and CERES data during

2003–2006, and showed that the 4-year mean values of the instantaneous SW, LW, and net CRFs are -138.9 , $+69.1$, and -9.7 Wm^{-2} , respectively, in dust-contaminated cloudy regions. However, to date, the cloud shortwave or longwave RF on regional climate in Taklimakan Desert has remained unknown, due to lack of accurate observations of terrestrial solar radiation, cloud microphysical and macrophysical parameters, as well as the profiles of aerosol, air temperature, and humidity.

To improve our understanding of the dust-cloud-precipitation feedbacks and related regional climate impacts over Taklimakan Desert and its surrounding areas, the Semi-Arid Climate and Environment Observatory of Lanzhou University (henceforth SACOL, <http://climate.lzu.edu.cn/english/>) and Institute of Desert Meteorology, China Meteorological Administration (CMA) jointly initiated an intensive field experiments in Tarim Basin during summer of 2019. There are two sites deployed during the intensive period. Tazhong, a super and permanent site (38.968°N , 83.659°E , 1100 m above MSL), is situated in the hinterlands of the Taklimakan Desert, which is set up with an 80-m gradient meteorological tower, surface radiation instruments, eddy covariance system, air quality monitoring instruments, two-wavelength polarization and Raman lidar, CHM15k ceilometer, and sun-sky radiometer. Another site at Minfeng Country Bureau of Meteorology (37.067°N , 82.691°E , 1408 m above MSL) is located in the southern part of the Taklimakan Desert, which is regarded as an active center of dust storms in the world. A terrestrial radiation site and an automatic weather station were established at Minfeng during the experiment. This study primarily analyzed the surface radiation characteristics and evaluated the downward cloud radiative effects based on high-precision measurements of broadband radiometers in Minfeng, a southern Xinjiang during the summer 2019. The main structure of this article is arranged as follows. Section 2 introduces the site information and instruments. Section 3 depicts the identification method of clear-sky conditions and the calculation of the downwelling cloud radiative forcing. The results and analysis are given in Sect. 4 and followed by the conclusion and discussions in Sect. 5.

2 Site and instrumentation

2.1 Site information

Minfeng is situated at the northern foot of Kunlun Mountain and the southern margin of Taklimakan Desert, which is a tiny isolated oasis encompassed by Great desert and arid zones. The climatic pattern of the region is a typical temperate desert climate. The annual average temperature here is about 11.1°C , with large diurnal and annual variations. The annual mean rainfall is only 30.5 mm, approximately 65%

of which appears in summer, and the average evaporation is greater than 2750 mm. The mean wind speed is 1.61 ms^{-1} , with a maximum of 2.19 ms^{-1} in spring. The annual total sunshine duration is approximately 2840 h (Sourced from the China Meteorological Administration). The annual average days of dust storm, blowing dust, and floating dust are about 34, 78, and 178, respectively, which mainly occur in spring and summer seasons (Aili 2012).

2.2 Automatic weather station

An automatic weather station is established nearby the observation site of Minfeng Country Bureau of Meteorology, which could continuously collect multiple meteorological variables. A temperature and humidity probe (HMP155A, Vaisala, Finland) is designed to detect the air temperature (T_{air} in $^{\circ}\text{C}$) and relative humidity (RH in %), with the accuracies of $\pm 0.2 \text{ }^{\circ}\text{C}$ and $\pm 1\%$, respectively. A wind sensor (034B-L, Met One, USA) can simultaneously measure the wind speed (WS in ms^{-1}) and wind direction ($^{\circ}$), with the accuracies of $\pm 0.3 \text{ ms}^{-1}$ and 0.1° , respectively. The ambient pressure (P in hPa) is observed by a barometric pressure sensor (CS100, Setra, USA) from 600 to 1100 hPa range, with an accuracy of 0.1 hPa. And a tipping-bucket rain gauge (52,203, YOUNG, USA) can be capable of measuring the total precipitation (mm), with the resolution and accuracy of 0.1 mm and $\pm 2\%$, respectively. All above-mentioned sensors are mounted on a 2-m height horizontal bracket, which are unobstructed by the surrounding obstacles as far as possible. The saturation vapor pressure and vapor pressure (e in hPa) are calculated via an approximating polynomial formula and the observed T_{air} and RH, as recommended by Lowe (1977).

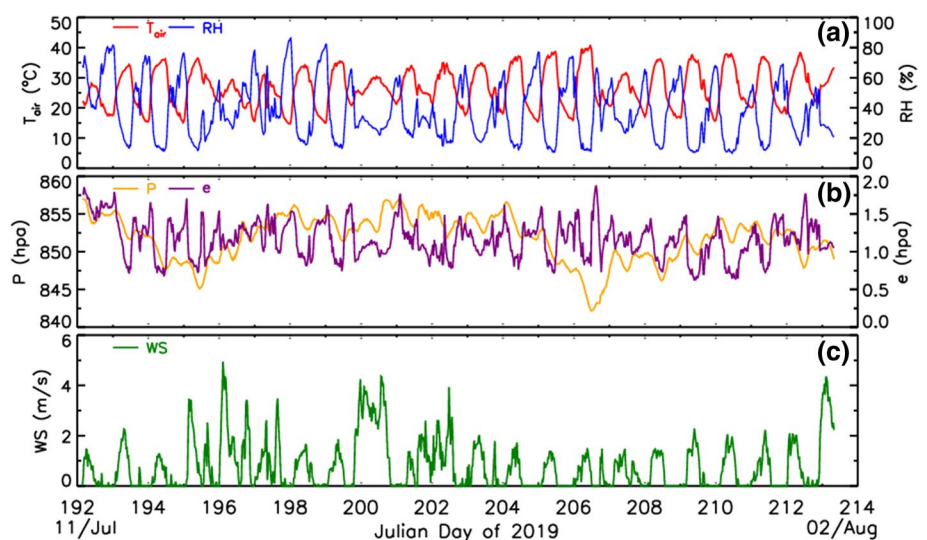
During the whole experiment, the overall mean air temperature (T_{air}) is $26.6 \pm 6.3 \text{ }^{\circ}\text{C}$ (mean \pm standard deviation, as seen in Fig. 1), which is about $2.2 \text{ }^{\circ}\text{C}$ larger than that of the

multi-year average value in summer (Aili 2012). The mean relative humidity (RH) is $37.8 \pm 18.7\%$, and about 59% of the total RH data points are greater than 40%. The ambient pressures commonly vary between 850 and 857 hPa and vapor pressures range from 0.60 to 1.90 hPa. Two evident low-pressure processes appear on July 14 ($\sim 845 \text{ hPa}$) and July 26 ($\sim 842 \text{ hPa}$), which suggests the passage of cold frontal cyclones. The mean wind speed (WS) is $0.81 \pm 1.0 \text{ ms}^{-1}$, with 34% of WS greater than 1.0 ms^{-1} . The wind rose diagrams represent the wind direction frequencies in diverse directions, as shown in Fig. 2. A distinct southwest and southerly wind is dominated for the entire period, and corresponding wind speeds are mostly less than 5.0 ms^{-1} (see Fig. 2a). In the nighttime (22:00–08:00 local time), the predominant southwest and southerly wind is more significant and most of wind speeds are smaller than 1.0 ms^{-1} (Fig. 2c), which can be explained via classical mountain wind circulation from southern huge Kunlun mountain. In the daytime (09:00–21:00 local time), wind directions might come from various orientation, although the southwest and northeast winds appear to be predominated. Moreover, the southerly wind speeds exhibit much greater than that from northerly wind, as described in Fig. 2b.

2.3 Terrestrial solar radiation measurements

An array of state-of-the-art broadband radiometers was mounted on a solid horizontal platform of a two-axis solar tracker (SOLYS-2, Kipp&Zonen, The Netherlands) where the field of view was not blocked in all directions. The downward solar shortwave radiation (or total solar radiation, $0.285\text{--}2.8 \text{ }\mu\text{m}$) and longwave radiation (infrared or thermal radiation, $3.5\text{--}50 \text{ }\mu\text{m}$) fluxes were, respectively, measured via a ventilated spectral pyranometer (Model PSP, Eppley Lab.) and a ventilated and shaded pyrgeometer (Model PIR,

Fig. 1 Time series of 30-min averaged **a** air temperature (T_{air} in $^{\circ}\text{C}$) versus relative humidity (RH in %), **b** ambient pressure (P in hPa) versus vapor pressure (e in hPa), and **c** wind speed (WS in m/s) at Minfeng site during the whole period of the field experiment



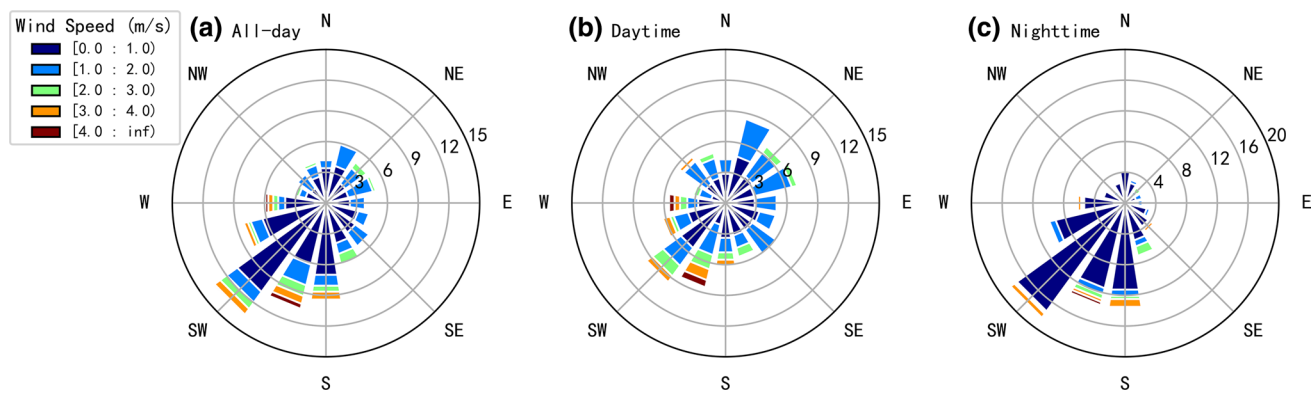


Fig. 2 Wind rose diagrams for **a** All-day, **b** Daytime (09:00–21:00 Beijing Time), and **c** Nighttime (22:00–08:00 Beijing Time) at Minfeng site during the entire period. Different color bars represent different levels of wind speed

Eppley Lab.). And the solar direct and diffuse radiation fluxes were independently detected via a normal incident pyrheliometer (Model NIP, Eppley Lab.) and a ventilated and shaded PSP pyranometer. All broadband radiometers completely conformed to the World Meteorological Organization (WMO) second-level observational standards. The SOLYS-2 solar tracker is an all-weather positioning and specialized instrument used to automatically point at the sun's movement across the sky, with a pointing accuracy of 0.05° , which meets with the Baseline Surface Radiation Network (BSRN) requirements. All aforementioned radiative fluxes and meteorological variables were automatically collected and saved in a Campbell data logger with 1-min and 30-min resolutions. Meanwhile, the observers manually recorded the cloud type, total cloud cover, weather condition, and visibility every 1 h during the daytime, which could help to identify important weather processes, for instance, dust storm, clear-sky, cloudy, or rainy days.

3 Methodology

3.1 Cloud radiative forcing calculation

Cloud radiative forcing (or cloud radiative effect) in this study is defined as the difference between the measured downward radiation flux and that expected for the clear-sky conditions (Ramanathan et al. 1989; Long and Ackerman 2000). There are usually two methods to calculate the expected surface shortwave (SW) or longwave (LW) radiative fluxes under clear-sky conditions, the model simulation, and empirical fitting algorithm. The radiative transfer models generally require some key input parameters, such as aerosol amount, air temperature and relative humidity profiles, and spectral surface reflectance (Bi et al. 2013, 2014), which are not readily available in many circumstances, especially in the Taklimakan Desert region. It has verified

that the solar zenith angle (SZA) is the primary factor for determining the magnitude of the diurnal cycle of downward shortwave radiation under cloudless conditions, and the columnar aerosol optical depth, water vapor content, and surface albedo exhibited far less influences (Long and Ackerman 2000). Therefore, it is customary to empirically fit the clear-sky shortwave radiation fluxes using the cosine of SZA as the independent variable, for instance, a linear fit (Cess et al. 1995), a polynomial fit (Waliser et al. 1996; Khatri and Takamura 2009), and a simple power law fit (Long and Ackerman 2000). Once the downward clear-sky shortwave radiation is determined, we could easily calculate the downwelling cloud radiative forcing according to its definition.

3.2 Clear-sky identification

Long and Ackerman (2000) developed an effective and automated method for identifying the periods of clear skies for a 160° field of view based on 1-min resolution of surface total and diffuse shortwave radiation measurements, which was proved to be robust and reasonable using the lidar data, Whole Sky Imager, and model comparisons. Here, a brief description of the clear-sky detection method is introduced. The algorithms mainly tested the total and diffuse shortwave radiation measurements with 1-min resolution for magnitude, variability, and change in magnitude with time and differentiated the cloudless or cloudy conditions. That is, the clear-sky detection procedure primarily included four tests: (1) normalized total shortwave magnitude test, (2) maximum diffuse shortwave test, (3) change in magnitude with time test, and (4) normalized diffuse ratio variability test.

The first test is designated the normalized total shortwave radiation as the downward total shortwave radiation divided to the power law function of the cosine of the SZA (μ_0) and set the maximum and minimum limits, which are designated as 1150 Wm^{-2} and 850 Wm^{-2} , respectively. Those normalized values falling within the range were tentatively marked

as cloudless. The first test mainly eliminates the early morning and late evening times for clear-sky detection for SZA greater than 80° , and, in other words, discards the periods of apparent positive and negative cloud effect. The maximum diffuse shortwave test is to compare the measured downward diffuse radiation to certain diffuse limit (D_{\max}), which was subjectively set and depended on the locations and their climatological clear-sky diffuse radiation. In this study, the D_{\max} is set at 200 Wm^{-2} for Minfeng site according to the results discussed in Sect. 3.1. The second test majorly eliminates the obvious periods of cloudiness, thick haze, or sub-visual cirrus conditions. The change in magnitude with time test is to compare the change in observed total shortwave radiation to the corresponding change of radiation at the top of the atmosphere, which mainly detected the more subtle variation of cloudiness. For the clear-sky circumstances, the change in measured total shortwave irradiance should be less than the corresponding change in the top-of-atmosphere. The diffuse ratio is defined as the ratio of diffuse radiation to total shortwave radiation, which is sensitive to the subtle changes in both direct and diffuse shortwave radiations. And the fourth test is the normalized diffuse ratio variability test, which sets a clear-sky detection limit value of 0.0015 for the standard deviation of an 11-min period of the normalized diffuse ratio. This test is primarily to eliminate the optically thin clouds or partly cloudy skies. Long and Ackerman (2000) pointed out that each individual test is not sufficient to assure whether the skies were clear or not, and only the data points passed all four-step screening are deemed representative of clear-sky conditions.

4 Results and analysis

4.1 Surface radiation characteristics

To understand intuitively the characteristics of surface radiation over southern Xinjiang, we first analyze the diurnal variations of terrestrial solar radiation fluxes under three typical weather conditions. Based on the hourly manual records, we can distinguish roughly the clear-sky (25 July), dusty (31 July), and cloudy (15 July) conditions, as illustrated in Fig. 3. As mentioned above, the SZA is the predominant factor that affects the magnitude of downward shortwave radiation under cloudless conditions. Therefore, the diurnal variations of clear-sky surface shortwave irradiances exhibit a smooth and symmetrical pattern, and the maximum appears at local noon time, with peak values of 915.6, 921.2, and 121.9 Wm^{-2} , respectively for total, direct and diffuse shortwave radiations on 25 July 2019. Our results are clearly smaller than those in Taklimakan Desert hinterland (He et al. 2008), attributed to the potential influences of more cloudy or dusty weather processes in Minfeng. Figure 3 shows that

direct radiations drastically decrease and diffuse radiative fluxes significantly increase under dusty and overcast days. It is worth noting that the diurnal variations present a relatively gentle fluctuation under dusty conditions, while corresponding variations exhibit a very sharp fluctuation under cloudy cases, mainly owing to the different intensities of scattering and reflection by airborne dust particles or cloud droplets. The overall means of direct shortwave radiation in daytime are markedly reduced by about 326.6 Wm^{-2} and 404.7 Wm^{-2} , respectively, by dust particles and cloud droplets, while corresponding diffuse radiations are increased by about 142.3 Wm^{-2} and 64.9 Wm^{-2} . Consequently, the overall attenuation effects on daytime total shortwave radiation are approximately decreased by 68.2 Wm^{-2} and 198.0 Wm^{-2} , respectively, by dust and cloud particles. The diurnal variation of downward longwave radiation is predominantly dependent on the clouds, water vapor, CO_2 , and aerosol particles (Wang and Dickinson 2013). Similarly, the clear-sky longwave radiative fluxes display small diurnal variation and relatively smooth with time, ranging from 446.6 Wm^{-2} to 478.4 Wm^{-2} . However, the diurnal variations of longwave radiation under dusty and cloudy circumstances display high values and distinct fluctuation. This implies that the occurrences of dusty layer or cloudy layer could substantially enhance the downward longwave radiation. In general, the averaged longwave radiative fluxes are increased by 41.5 Wm^{-2} and 71.9 Wm^{-2} , respectively, by dust and cloud particles. As a result, the overall downward radiative effects (the sum of shortwave and longwave) by dust or cloud are significantly negative.

Based on the aforementioned hourly manual records and diurnal variations of measured terrestrial radiations, it is clear that 25 July is a completely clear-sky day, and the other 5 days (July 13, 17, 18, 23, 24) are partly cloudless. There are distinct two dusty days for July 12 and 31, and the other days are obviously cloudy or overcast sky. This supplies us invaluable datasets to explore the downward cloud radiative forcing in southern Xinjiang. Figure 4 depicts the time series of 1-min averaged surface shortwave and longwave radiations and diffuse ratio at Minfeng site during the whole period. The day-to-day and diurnal variations of surface shortwave and longwave irradiances show a prominent pattern, which are remarkably affected by the occurrences of cloudy or dusty conditions. The clear-sky total and direct shortwave radiations present a smooth and symmetrical feature, whereas they are drastic fluctuations and significantly decrease under cloudy or dusty days. The diffuse radiations under cloudless conditions are commonly smooth and remain low values, with the maximum ranging from 120 to 200 Wm^{-2} , which could be regarded as a reference for the maximum limit of diffuse radiation at Minfeng site, as mentioned in Sect. 2.2. The downward longwave radiation with corrected by case and dome temperatures is slightly

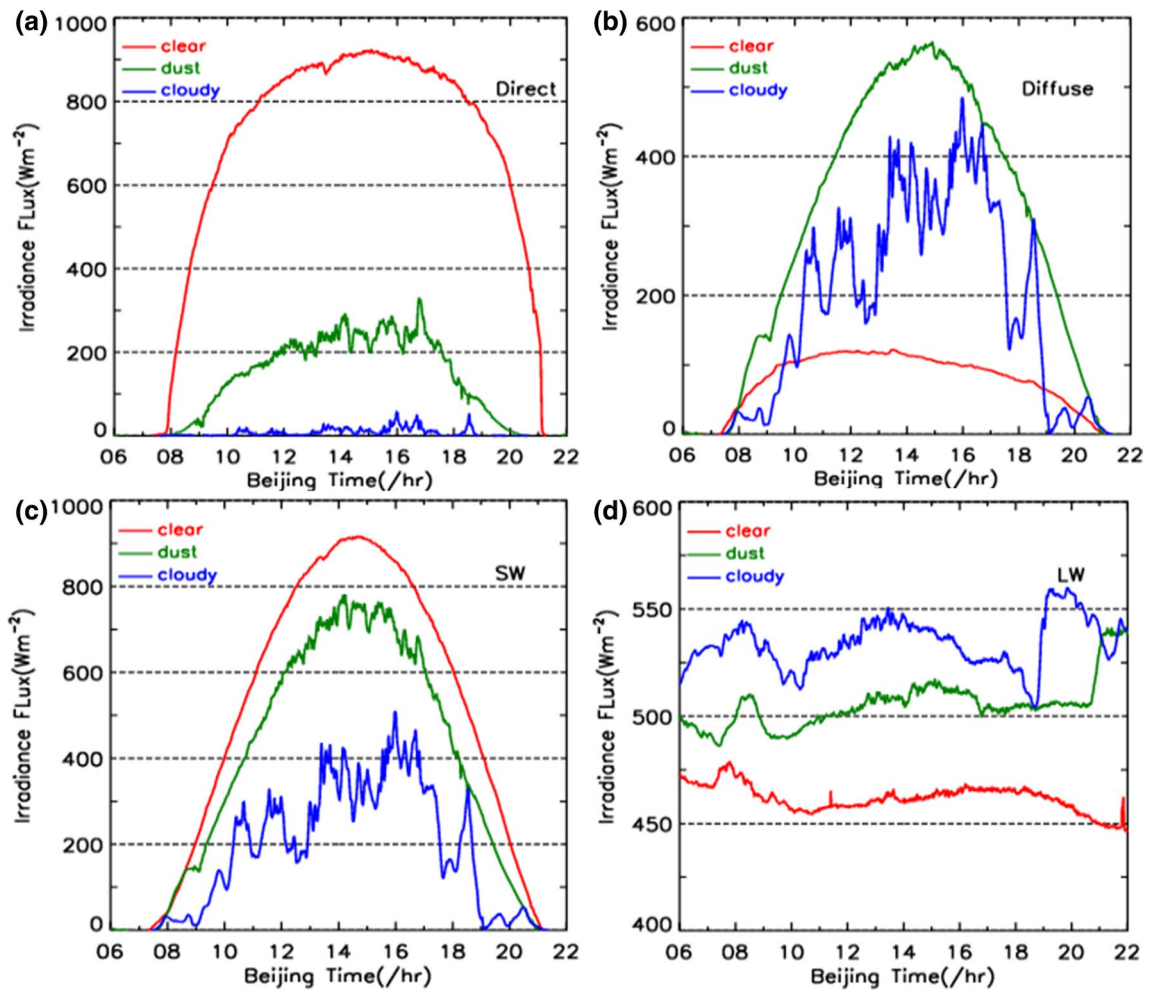
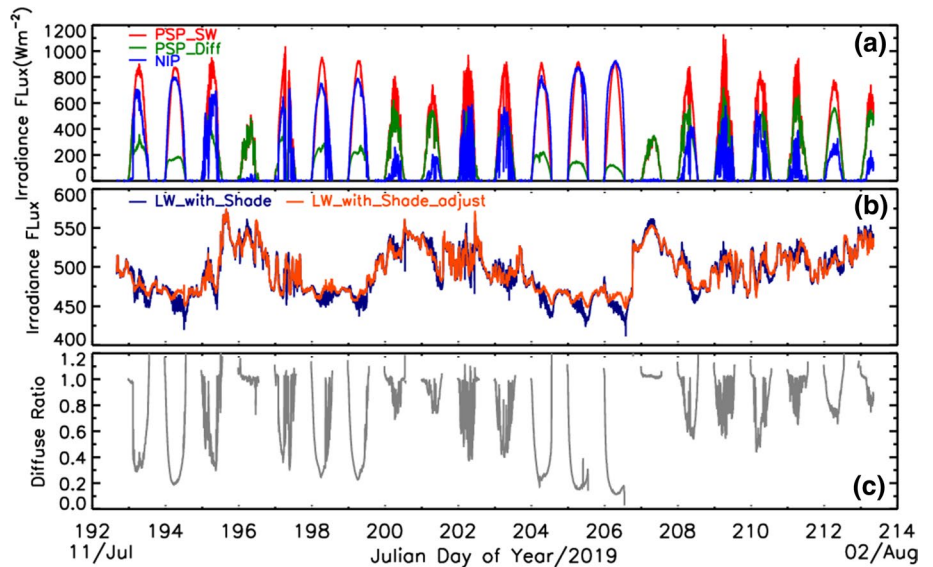


Fig. 3 Diurnal variations of **a** direct shortwave radiation, **b** diffuse radiation, **c** total shortwave radiation, and **d** downward longwave radiation fluxes (unit: Wm^{-2}) under three typical weather conditions.

Red is clear-sky (July 25), green is dusty (July 31), and blue is cloudy (July 15) condition

Fig. 4 Time series of 1-min averaged **a** total shortwave radiation (PSP_SW), diffuse radiation (PSP-Diff), and direct shortwave radiation (NIP) fluxes in Wm^{-2} , **b** downward longwave radiation fluxes with (deep blue) and without (red) adjust of temperature compensation, and **c** diffuse ratio (=diffuse/total shortwave radiation) during the whole period



less than that without adjust, both of which are equipped with a shading ball. The longwave irradiances range from 425 to 575 Wm^{-2} during the entire period. The diffuse ratio is very sensitive to the subtle changes in both diffuse and direct shortwave irradiances and is an important quantity for identifying clear-sky and cloudy conditions. From Fig. 4c, it is noteworthy that the diurnal variations of diffuse ratio under clear-sky condition are also smooth and symmetrical, which are usually smaller than 0.30. And the diffuse ratios under cloudy or dusty conditions present dramatic fluctuations and keep relatively high values, which are generally greater than 0.40. For instance, the diffuse ratios under overcast sky vary from 0.8 to 1.0 range and vary from 0.6 to 1.0 under dusty days.

4.2 Clear-sky identification results

As stated above, the diurnal variations of total, direct, and diffuse shortwave radiation characteristics under cloudy conditions exhibit evidently different patterns from those under

cloudless conditions. In this study, we make use of a series of four tests to eliminate the cloudy data and efficiently identify the clear-sky condition, as recommended by Long and Ackerman (2000). Figure 5 delineates the screening results of clear-sky identification for 25 July 2019 based on 1-min measurements of total and diffuse shortwave radiation at Minfeng. After a rigorous four-step screening algorithm, almost all the data points in daytime passed the clear-sky identification tests, which is consistent with the fact that 25 July is a complete clear-sky and clean day. Figure 6 is the same as Fig. 5, but for 24 July 2019 at Minfeng site. Combined the ground-based measurements and hourly manual records, there are partly clouds appeared in the afternoon on 24 July 2019. From Fig. 6, except for the second test (i.e., Maximum diffuse shortwave test), the other three screening tests could be fairly detected and eliminated the obvious periods of cloudiness (i.e., 17:34–17:54 local time) on 24 July 2019, which is probably ascribed to the maximum diffuse limit was set too high ($D_{\max} = 200 \text{ Wm}^{-2}$) in the second test. It is apparent that the first two tests could not probe the

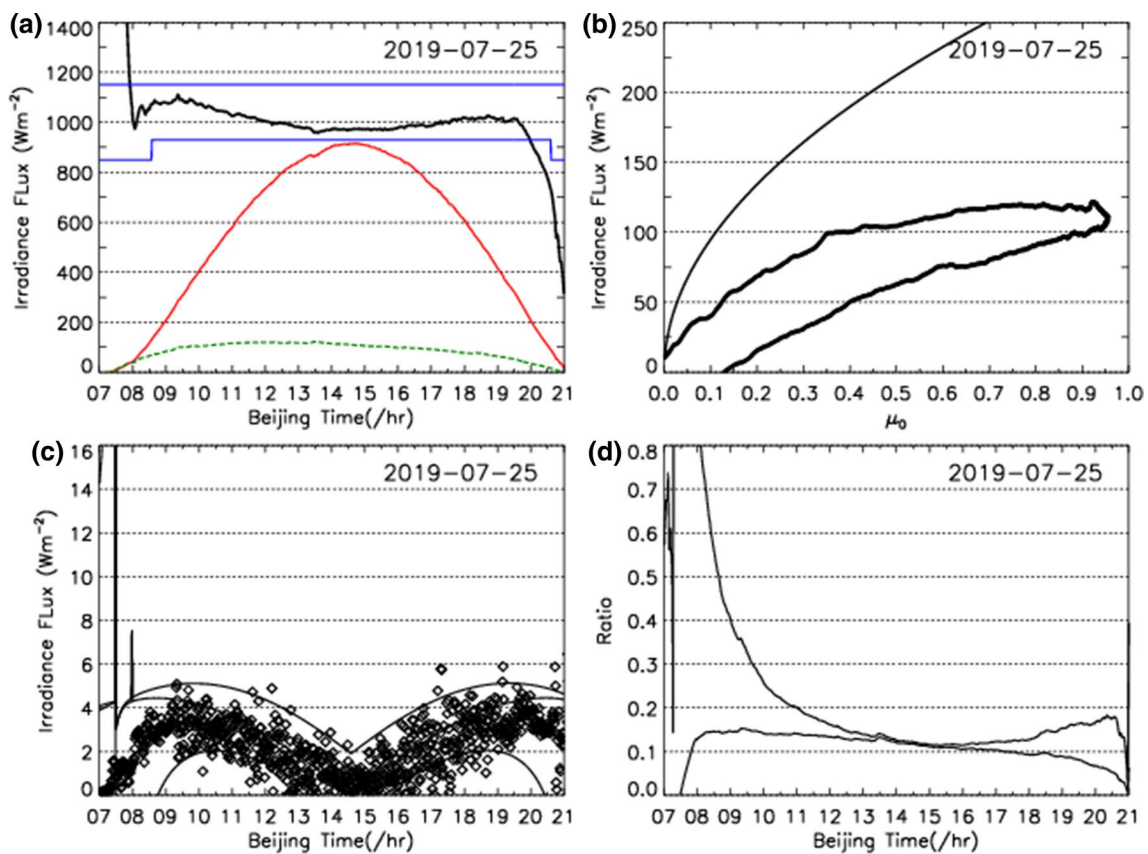


Fig. 5 Four tests for clear-sky identification method recommended by Long and Ackerman (2000) for a complete clear-sky day (July 25, 2019). **a** Measured total (red solid line) and diffuse (green dotted line) shortwave irradiances. Heavy black line is the normalized total shortwave radiation; heavy blue lines are the normalized maximum and minimum limits. **b** Thin black line is the clear-sky diffuse limit and

diamonds are the measured diffuse radiation. μ_0 is the cosine of the solar zenith angle. **c** Diamonds represent the change of measured total shortwave radiation, and gray lines are the clear-sky envelope. Solid black line is the change of the top-of-atmosphere. **d** Time series of diffuse ratio (heavy line, top) and normalized diffuse ratio (thin line, bottom)

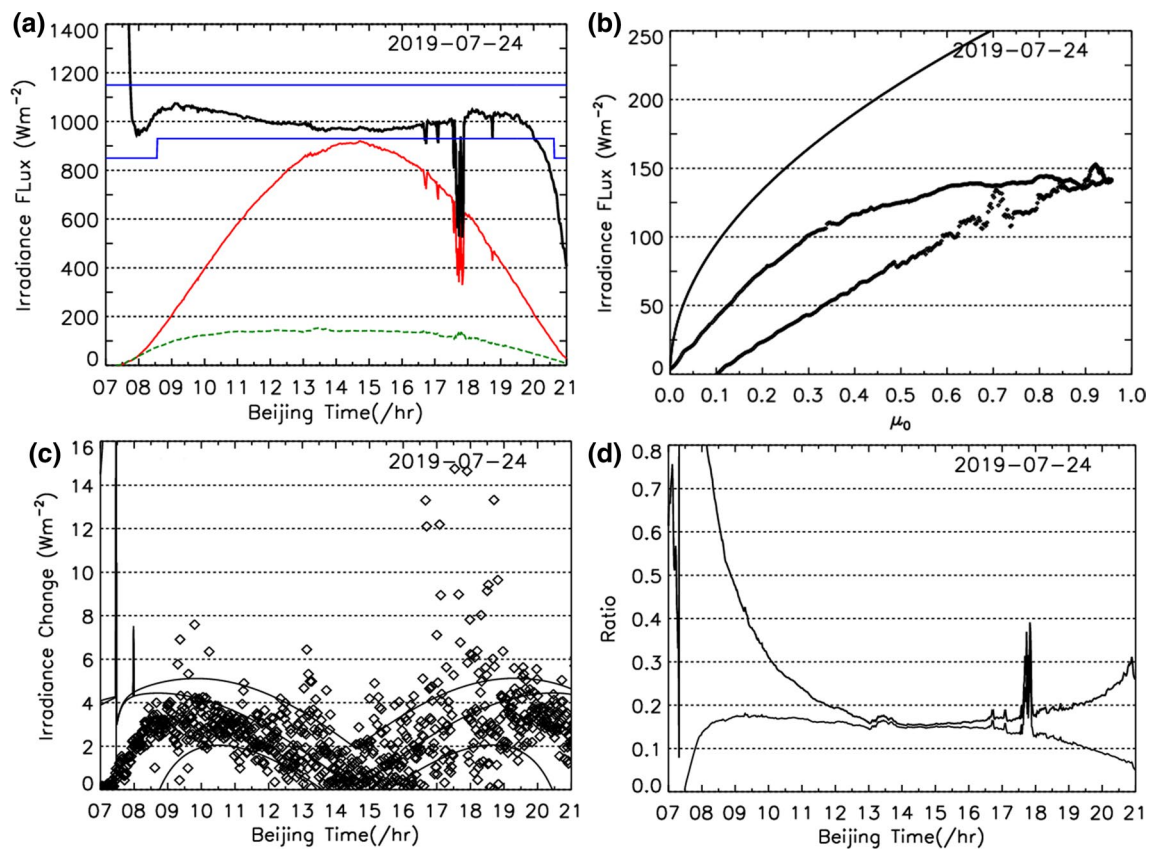


Fig. 6 The same as Fig. 5, but for July 24, 2019. There are some clouds occurred in the afternoon on July 24, 2019

subtle changes of optical thin clouds, but both the change in magnitude of total radiation test and normalized diffuse ratio variability test could successfully identify and eliminate these subtle variations of cloudiness (i.e., 16:40–16:45, 17:04–17:07, and 18:43–18:47 local time) on 24 July 2019, as shown in Fig. 6.

Figure 7 draws several cases of the measurements identified as clear-sky superposed on the downward total shortwave radiation for July 13, 17, 24, and 25, 2019 at Minfeng site. Both the obvious and subtle changes of cloudiness in daytime are fairly detected and identified for selected 4 different days after rigorous four-step screening tests. That is, any slight perturbations of total solar radiation induced by clouds are efficiently recognized, which demonstrates that the clear-sky identification method used in this study is robust and reliable.

4.3 Empirical fitting of clear-sky radiation

As mentioned above, solar shortwave radiation under cloudless conditions can be empirically fitted using the cosine of SZA (μ_0) as an independent variable. Here, we use a power law equation to fit the clear-sky total and diffuse shortwave radiations. And the expression is given as follows:

$$Y = a \times \mu_0^b, \quad (1)$$

where Y is the total solar radiation or diffuse ratio under clear-sky conditions, and a and b denote the regression coefficients. Compared with a linear fit or a polynomial fit, the formula (1) includes some simple physical implications. The coefficient a represents the clear-sky radiation flux for a SZA of 0° and contains the influences of radiometer calibration, the average columnar aerosol loading and water vapor amounts, and the Earth-Sun distance on that day. The coefficient b contains the effects of cosine response of the radiometer. The regression coefficients (i.e., a and b) are calculated via using a least-squares estimation that minimizes the sum of the absolute deviations. Moreover, a minimum number of identified clear-sky measurement in this method is set to 120, which primarily ensures that the clear-sky measurement datasets cover a large range of SZAs and assures a statistically rigorous calculation. The correlation coefficients R^2 are 0.99913 and 0.99897 for July 24 and 25 clear-sky total shortwave radiations, respectively, and with corresponding values of 0.93436 and 0.91330 for clear-sky diffuse ratios, respectively.

Table 1 summarizes the daily regression coefficients (a and b) for the clear-sky diffuse ratio and total shortwave

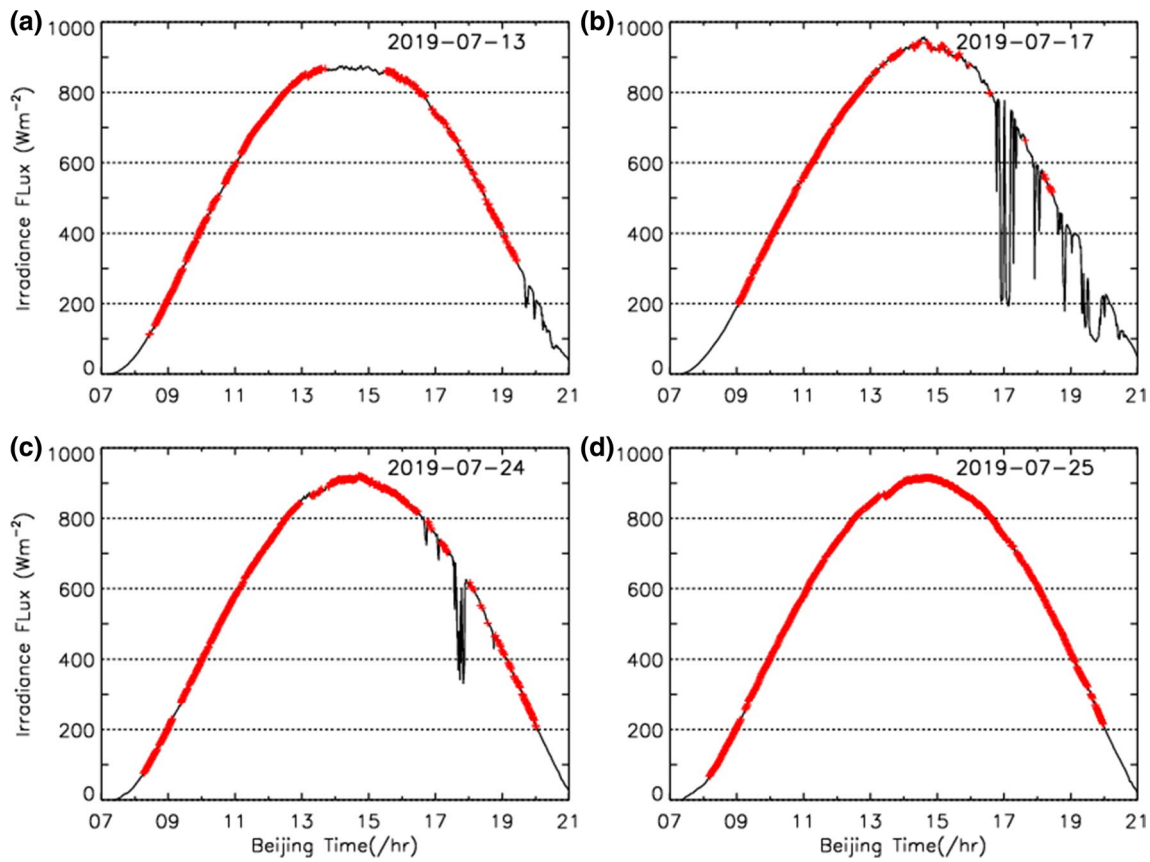


Fig. 7 Measurements identified as clear-sky (red crosses) superposed on the downward total shortwave radiation (black line) on **a** July 13, **b** July 17, **c** July 24, and **d** July 25, 2019

Table 1 Daily regression coefficients (a and b) for the clear-sky diffuse ratio and total shortwave radiation on July, 2019 at Minfeng site

Date	DifRat a	DifRat b	Total SW a	Total SW b	N
July 13, 2019	0.184	-0.965	951.573	1.273	356
July 17, 2019	0.269	-0.792	958.233	1.316	269
July 18, 2019	0.235	-0.914	958.466	1.293	298
July 23, 2019	0.224	-0.682	945.744	1.316	178
July 24, 2019	0.149	-0.789	968.276	1.267	450
July 25, 2019	0.111	-0.882	966.202	1.250	607
AVG	0.195	-0.837	958.082	1.286	

DifRat is the clear-sky diffuse ratio; total SW is total shortwave radiation; N is the number of 1-min measurements identified as clear skies for that day; AVG is the overall mean value

radiation on July, 2019 at Minfeng site. It is distinct that the minimum number of identified clear-sky observations on July 23 is 178, which sufficiently meets the requirements of statistical calculation. The regression coefficients of diffuse ratio vary from 0.111 to 0.269 and -0.965 to -0.682 for a and b constants, respectively, with a variation of ~30–41% of the largest-magnitude value. And the regression coefficients of total shortwave radiation vary from 946 Wm⁻² to

968 Wm⁻² and from 1.250 to 1.316 for a and b, respectively, with the corresponding variation of ~2–5% of the largest-magnitude value for both coefficients. Therefore, the overall mean of regression coefficients (a and b) for the clear-sky diffuse ratio and total shortwave irradiance on July of 2019 are 0.195, -0.837, 958.082, and 1.286, respectively. As long as the regression coefficients are reasonably determined, we could reliably estimate the clear-sky total and diffuse shortwave radiation fluxes according to the formula (1).

Figure 8 outlines the time evolutions of measured and clear-sky fitted total radiation and diffuse radiation fluxes for four different sunny days. Generally, the fitted total and diffuse shortwave radiations under clear-sky conditions agree well with the ground-based measurements in magnitude and diurnal variations, which directly confirms that the power exponential fitting methods in this study is reliable. From Fig. 8, compared with the surface measurements, the fitting irradiances seem to slightly overestimate the total radiation near noon and during the late-afternoon, and slightly underestimate the diffuse radiation during the midmorning and slightly overestimate during the midafternoon. This may be mainly ascribed to the influences of the cosine response of the pyranometers at different time periods.

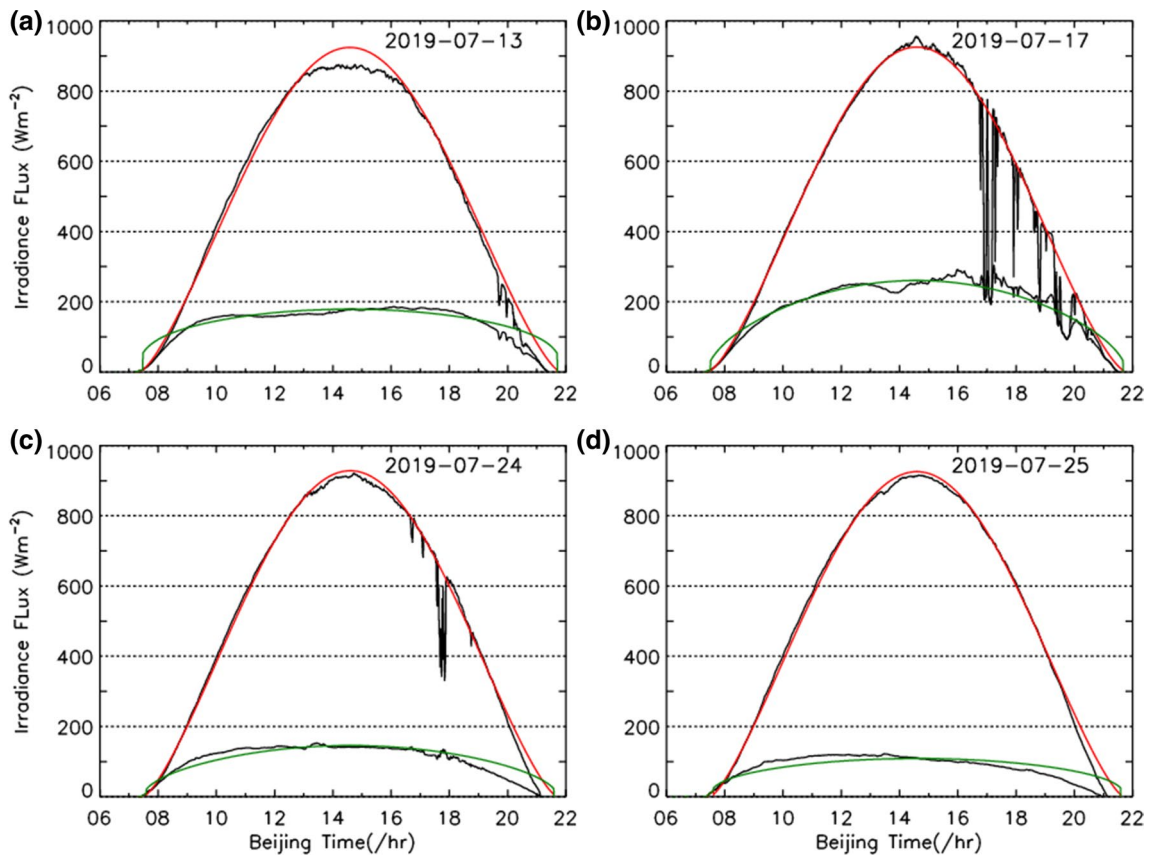


Fig. 8 Time series of measured (heavy black line) and clear-sky fitted (red line) total shortwave radiation; measured (gray line) and clear-sky fitted (thin green line) diffuse radiation for **a** July 13, **b** July 17, **c** July 24, and **d** July 25, 2019

Figure 9 depicts the intercomparisons between the fitted and ground-based measured total and diffuse shortwave radiations under cloudless conditions at Minfeng site during the whole period. There are 2161 points of 1-min clear-sky

irradiance for comparisons. In general, the fitted total shortwave radiations under clear-sky cases are perfectly consistent with the ground-based measurements, with the correlation coefficient R^2 of 0.999. The fitted total SW radiations

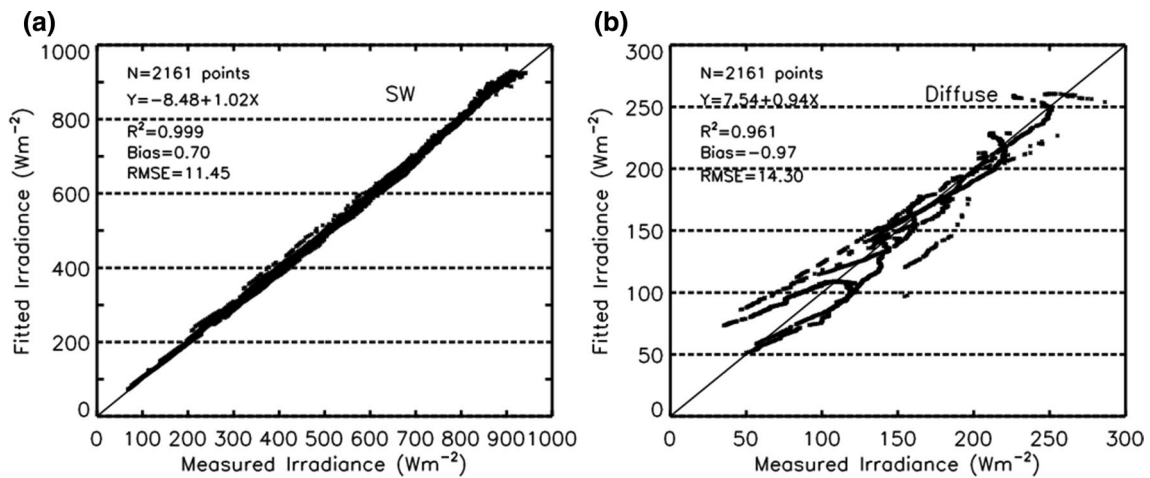


Fig. 9 Intercomparisons between the clear-sky fitted and ground-based measured irradiances for **a** total shortwave radiation (SW, in Wm^{-2}) and **b** diffuse radiation (Diffuse, in Wm^{-2}). The 1:1 black solid line is shown for comparison

present a slight overestimation with a mean difference (Bias) of about 0.70 Wm^{-2} and root-mean-squared error (RMSE) of 11.45 Wm^{-2} . And the fitted diffuse irradiances seem to be somewhat underestimated, with the corresponding R^2 , Bias, and RMSE of 0.961, -0.97 Wm^{-2} , and 14.30 Wm^{-2} , respectively. Both the RMSE uncertainties fall within the nominal accuracy ($\sim 15 \text{ Wm}^{-2}$) of measured total and diffuse shortwave radiations by pyranometer descended from cosine response and calibration.

Figure 10 shows the downward total SW radiative fluxes at Minfeng during the July 2019. The thick red curve is the downwelling total SW radiation at the top of the atmosphere (TOA), the green curve is the fitted clear-sky SW radiation, and the dots are the 1-min ground-based measured total SW fluxes. It is distinct that both the fitted and measured surface SW radiations are smaller than the total SW radiation at the TOA, which is expected. There are some points greater than the fitted clear-sky SW radiation, reflecting a positive SW effect of cloud due to the enhancement of diffuse SW radiation by clouds. Obviously, most measured total SW radiations are less than the fitted clear-sky SW fluxes, indicating the negative cloud effect ascribed to the attenuation of direct SW radiation by clouds. We define the transmittance of the atmosphere as the ratio of the fitted clear-sky SW radiation to the total SW radiation at the TOA. The transmittance of the atmosphere is about 0.59 for $\mu_0 \approx 0.50$ and 0.68 for $\mu_0 \approx 0.90$. Thereby, the maximum values of the surface SW radiation alone could not supply adequate information for identifying clear-sky fluxes under strong convective regions.

4.4 Cloud radiative effects

As stated above, the downward SW (or LW) cloud radiative forcing (CRF) can be calculated by the discrepancy between

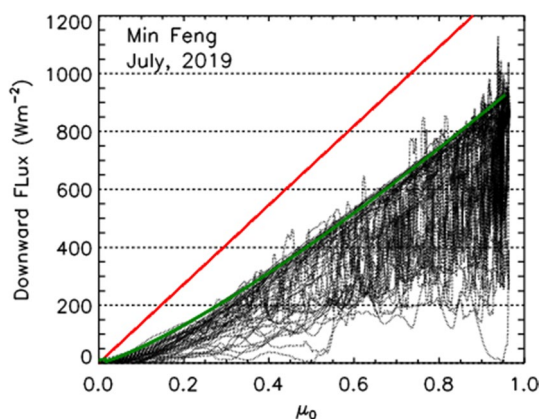


Fig. 10 The downward total SW radiative fluxes at Minfeng during July 2019. μ_0 is the cosine of the solar zenith angle. The thick red curve is the downwelling total SW flux at the top of the atmosphere, the green curve is the fitted clear-sky SW flux, and the dots are the ground-based measured total SW flux for 1-min resolution

the measured SW (or LW) radiation flux and the fitted clear-sky radiative flux. Hence, the cloud effect calculations in this study significantly decrease by the influences of the systematic offsets and cosine response errors of pyranometers, as well as the aerosol and water vapor amount. The fitted clear-sky SW radiation flux is determined according the aforementioned power law formula (1). In this paper, we determine the clear-sky periods of LW radiation in daytime according to the clear-sky detection method discussed in Sect. 2.2. And we roughly identify the clear-sky LW radiation in nighttime using the collocated measurements of Lidar, ceilometer, and the magnitude and diurnal variability of the LW radiation flux. As mentioned in Sect. 3, the clear-sky downward LW radiation shows small variation and relatively smooth with time, and we could set the magnitude of downward LW radiation under clear-sky condition as $400 \sim 480 \text{ Wm}^{-2}$ for Minfeng and the corresponding variability of standard deviation of LW flux with the last hours is less than 10 Wm^{-2} (Durr and Philipona 2004; Long and Turner 2008). Therefore, we obtain diurnal variations (including daytime and nighttime) of partially or completely clear-sky LW radiation flux, as shown in Fig. 11. To estimate the clear-sky LW radiation flux, we calculate the average diurnal cycles of all datasets of detected clear-sky LW radiations, which is extensively used in the applications of satellite remote sensing (Huang et al. 2006; Su et al. 2008). Consequently, the 24-h aggregate average downward SW (or LW) CRF can be determined through computing the diurnal cycles of 1-min downward SW (or LW) CRF.

Figure 12 shows the 24-h daily mean of downward CRF for SW, LW, and net cloud effect at Minfeng during July of 2019. The net cloud effect values are calculated from the sum CRF of downward SW plus the LW. On the regional

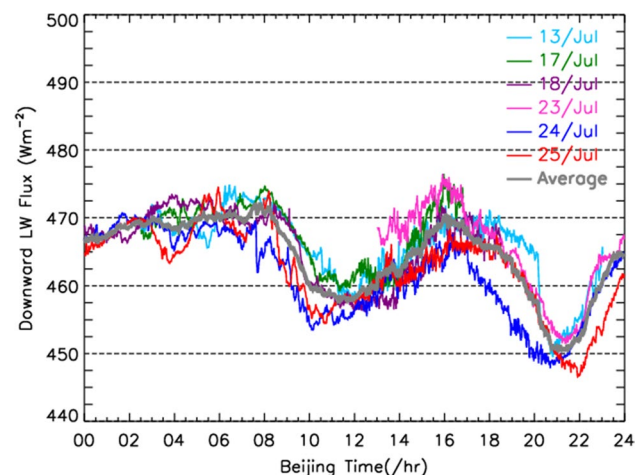


Fig. 11 Diurnal cycles of downward LW radiative fluxes under a few clear-sky days at Minfeng during July of 2019. Aggregate averages are marked as thick gray line

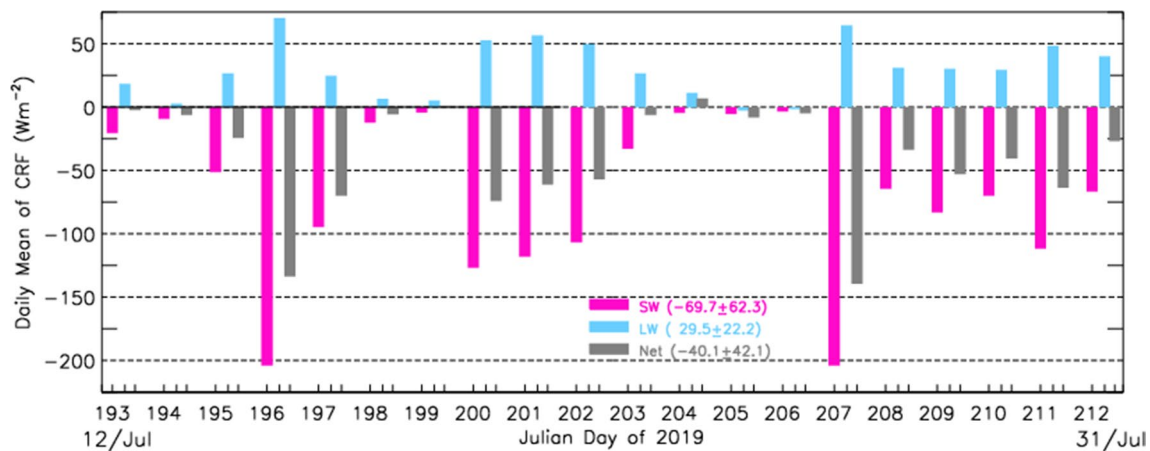


Fig. 12 Daily average values of downward cloud radiative forcings (CRF) for the total SW (pink bars) and LW (skyblue bars), and the net cloud effect (gray bars) at Minfeng during the July of 2019. Overall average values and one standard deviation are in parentheses

scale, the daily averaged SW CRFs are largely negative (-204.1 to -3.3 Wm^{-2}) and daily mean LW CRFs are moderately positive (-1.5 to $+70.4$ Wm^{-2}). Hence, the corresponding daily mean net cloud effects are negative (-139.6 to $+6.8$ Wm^{-2}) at Minfeng. Strong CRF values of downward SW and LW coincides with the overcast conditions or large cloud amounts. For example, the maximum and minimum CRF values of -204.1 Wm^{-2} and $+70.4$ Wm^{-2} for SW and LW, respectively, appear on 15 July 2019, which is an overcast and rainy day with total cloud cover of 10 (nimbostratus) due to the passage of cold frontal cyclones. In comparison, the radiative forcing values of SW, LW, and net radiative effects of dust aerosol on 31 July 2019 are -66.7 , $+40.0$, and -26.7 Wm^{-2} , respectively, which are 32.7%, 56.8%, and 19.1% of the corresponding values for the CRFs. Such a dramatic negative cloud radiative forcing of SW is about 1.7 times of the maximum sensible heat flux (~ 122.1 Wm^{-2}) observed in Taklimakan Desert region (Liu et al. 2012; Jin et al. 2018), which would undoubtedly exert a profound impact on the surface energy balance and the regional climate change. The overall averaged values of SW and LW CRFs and net cloud effect are -69.7 ± 62.3 , $+29.5 \pm 22.2$, and -40.1 ± 42.1 Wm^{-2} , respectively, implying that the clouds have a net cooling effect on the regional climate over southern Xinjiang during summer of 2019. Our result of SW cloud radiative forcing is consistent with the summer average of -70.9 Wm^{-2} in Xianghe, a rural site of northern China, but is smaller than that in Taihu (~ -89.1 Wm^{-2}) of southern China (Tang et al. 2011). Ramanathan et al. (1989) indicated that the global mean values of SW and LW CRFs and net cloud effect are -44.5 , $+31.3$, and -13.2 Wm^{-2} , respectively, suggesting that the regional net cooling effect is threefold as large as the global average. This negative cloud radiative forcing would partly counteract

the global warming induced by the well-mixed greenhouse gases and modulate the Earth's radiation budget balance.

5 Conclusion and discussion

This study primarily analyzed the surface radiation characteristics and evaluated downward cloud radiative effects based on high-precision measurements of broadband radiometers in southern Xinjiang during summer 2019. The main findings of this paper are summarized as follows.

Surface radiation fluxes show remarkable day-to-day and diurnal cycle variations and diverse clear-sky surface irradiances and diffuse ratio exhibit a smooth and symmetrical pattern, with the maximums of 915.6, 921.2, and 121.9 Wm^{-2} , respectively, for total, direct, and diffuse shortwave radiations on 25 July 2019. Cloud layer or dust layer could drastically decrease the surface total and direct shortwave radiations, but could significantly increase the diffuse and longwave radiations, which brings a strong downward negative radiative effect. Diffuse ratios under cloudless, overcast, and dusty conditions are commonly 0~0.3, 0.8~1.0, and 0.6~1.0, respectively, which is very sensitive to the subtle changes in both diffuse and direct shortwave radiations. We take advantage of a rigorous four-step screening algorithm to effectively identify the clear-sky and cloudy periods based on 1-min measurements of total and diffuse irradiances. The clear-sky total and diffuse shortwave radiations are empirically fitted using a power law equation, identified clear-sky measurements and the cosine of SZA. The clear-sky LW radiation is calculated via the average diurnal cycles of all datasets of detected 1-min clear-sky LW radiation. The 24-h daily mean CRFs are largely negative (-204.1 to -3.3 Wm^{-2}) for SW, and are moderately positive (-1.5 to $+70.4$ Wm^{-2}) for LW, which correspond to

the overcast conditions or large cloud amounts. The overall averaged values of SW and LW CRFs and net cloud effect are -69.7 ± 62.3 , $+29.5 \pm 22.2$, and $-40.1 \pm 42.1 \text{ Wm}^{-2}$, respectively, implying that the clouds have a net cooling effect on the regional climate. Our results are consistent with the summer average in northern China, but less than those in southern China, and greater than those of the global mean values.

Cloud radiative forcing is an essential part of the energy budget balance of the earth-atmosphere system. A comprehensive understanding of the complex cloud-climate feedback urgently needs to uncover the seasonal and interdecadal variations of cloud forcing over different regions. This conclusion is based on only 1 month ground-based dataset. Hence, in the future, long-term and continuous observations of surface radiative fluxes around China are crucial to elucidate its radiation characteristics and cloud radiative effects.

Acknowledgements This study was supported by the National Science Foundation of China (42075126), Project of Field Scientific Observation and Research Station of Gansu Province (18JR2RA013), and the Fundamental Research Funds for the Central Universities (lzujbky-2021-kb02, lzujbky-2021-sp04), and China 111 Project (No. B 13045). The authors would like to express special thanks to all staff of Minfeng Country Bureau of Meteorology for supporting the field experiment. We also appreciate all anonymous reviewers and editors for their constructive and insightful comments.

Data availability All the datasets used and analyzed in the current study are available from the corresponding author on reasonable request (Email: bijr@lzu.edu.cn).

References

- Aili I (2012) The analysis of climate change and dust aerosol in Niya, the south margin of Taklimakan desert. Master' thesis pp 25–30. (In Chinese)
- Bi J, Huang J, Fu Q, Ge J, Shi J, Zhou T, Zhang W (2013) Field measurement of clear-sky solar irradiance in Badain Jaran desert of Northwestern China. *J Quant Spectrosc Radiat Transf* 122:194–207
- Bi J, Huang J, Hu Z, Holben BN, Guo Z (2014) Investigating the aerosol optical and radiative characteristics of heavy haze episodes in Beijing during January of 2013. *J Geophys Res* 119(16):9884–9900
- Boucher O, Randall D, Artaxo P, et al (2013) Clouds and aerosols. In: Stocker TF, Qin D, Plattner G-K et al (eds) *Climate change 2013: the physical science basis. contribution of working group I to the fifth assessment report of the intergovernmental panel on climate change*. Cambridge University Press, pp 571–658
- Cess RD, Zhang M, Minnis P, Corsetti L, Dutton EG, Forgan BW, Garber DP, Gates WL, Hack JJ, Harrison EF, Jing X, Kiehl JT, Long CN, Morcrette J-J, Potter GL, Ramanathan V, Subasilar B, Whitlock CH, Young DF, Zhou Y (1995) Absorption of solar radiation by clouds: observations versus models. *Science* 267(5197):496–499
- Che H, Shi G, Zhang X, Arimoto R, Zhao J, Xu L, Wang B (2005) Analysis of 40 years of solar radiation data from China, 1961–2000. *Geophys Res Lett* 32(6):L06803. <https://doi.org/10.1029/2004GL022322>
- Chen Y, Peng K, Shi Y, Cui C, Lin X, Pan H (2009) Comparison of cloud water resources over Tianshan mountains and Taklimakan desert. *Arid Land Geogr* 32(6):886–891 (In Chinese)
- Durr B, Philipona R (2004) Automatic cloud amount detection by surface longwave downward radiation measurements. *J Geophys Res* 109:D05021. <https://doi.org/10.1029/2003JD004182>
- Dutton EG, Nelson DW, Stone RS, Longenecker D, Carbaugh G, Harris JM, Wendell J (2006) Decadal variations in surface solar irradiance as observed in a globally remote network. *J Geophys Res* 111(D19):D19101. <https://doi.org/10.1029/2005JD006901>
- He Q, Miao Q, Li S, Shi L, Ali M (2008) Global radiation characteristics and influencing factors of Taklimakan desert hinterland. *J Desert Res* 28(5):896–902 (In Chinese)
- Huang J, Minnis P, Lin B, Wang T, Yi Y, Hu Y, Sun-Mack S, Ayers K (2006) Possible influences of Asian dust aerosols on cloud properties and radiative forcing observed from MODIS and CERES. *Geophys Res Lett* 33(6):L06824. <https://doi.org/10.1029/2005G1024724>
- Jin L, Li Z, He Q, Liu Y, Ali M, Liu X, Huo W, Xin Y, Zhang J, Zhou C (2018) Observed key surface parameters for characterizing land-atmospheric interaction in the Northern marginal zone of the Taklimakan desert. *China Atmos* 9:458. <https://doi.org/10.3390/atmos9120458>
- Khatri P, Takamura T (2009) An algorithm to screen cloud-affect data for sky radiometer data analysis. *J Meteor Soc Jpn* 87(1):189–204
- Li J, Huang J, Wang T, Yi Y (2009) Analysis of vertical distribution of cloud in East Asia by space-based LiDAR data. *Chin J Atmos Sci* 33(4):698–707 (In Chinese)
- Li S, Hu L, He Q, Xu Z, Wu X (2012) Surface radiation budget in hinterland of the Taklimakan desert. *J Desert Res* 32(4):1035–1044 (In Chinese)
- Li J, Wang T, Habib A (2017) Observational characteristics of cloud radiative effects over three arid regions in the Northern Hemisphere. *J Meteor Res* 31(4):654–664
- Li J, Jian B, Huang J, Hu Y, Zhao C, Kawamoto K, Liao S, Wu M (2018) Long-term variation of cloud droplet number concentrations from space-based Lidar. *Remote Sens Environ* 213:144–161
- Li S, Hou X, Cui Y, Liang F, Xu Z (2019) Research on cloud characteristics based on FY-2F satellite data in Xinjiang region. *Plateau Meteorol* 38(3):617–624 (In Chinese)
- Liang F, Xia X (2005) Long-term trends in solar radiation and the associated climatic factors over China for 1961–2000. *Ann Geophys* 23:2425–2432
- Liou KN (1992) *Radiation and cloud processes in the atmosphere* [M]. Oxford University Press, New York, pp 172–248
- Liu YQ, He Q, Zhang HS, Ali M (2012) Improving the CoLM in Taklimakan desert hinterland with accurate key parameters and appropriate parameterization scheme. *Adv Atmos Sci* 29(2):381–390
- Long CN, Ackerman TP (2000) Identification of clear skies from broadband pyranometer measurements and calculation of downwelling shortwave cloud effects. *J Geophys Res* 105(D12):15609–15626
- Long CN, Turner DD (2008) A method for continuous estimation of clear-sky downwelling longwave radiative flux developed using ARM surface measurements. *J Geophys Res* 113:D18206. <https://doi.org/10.1029/2008JD009936>
- Lowe Paul R (1977) An approximating polynomial for the computation of saturation vapor pressure. *J Appl Meteorol* 16(1):100–103
- Mace G, Benson S, Sonntag K, Kato S, Min Q, Minnis P, Twohy CH, Poellot M, Dong X, Long C, Zhang Q, Doelling DR (2006) Cloud radiative forcing at the atmospheric radiation measurement program climate research facility. 1: technique, validation, and comparison to satellite-derived diagnostic quantities. *J Geophys Res* 111(D11):D11S90. <https://doi.org/10.1029/2005JD005921>

- McFarlane SA, Long CN, Flaherty J (2013) A climatology of surface cloud radiative effect at the ARM tropical western Pacific sites. *J Appl Meteorol Clim* 52:1006–1013
- Pinker RT, Zhang B, Dutton EG (2005) Do satellites detect trends in surface solar radiation? *Science* 308:850–854
- Ramanathan V, Cess R, Harrison E, Minnis P, Barkstrom BR, Ahmad E, Hartmann D (1989) Cloud-radiative forcing and climate: results from the earth radiation budget experiment. *Science* 243:57–63
- Shi G, Hayasaka T, Ohmura A, Chen Z, Wang B, Zhao J, Che H, Xu L (2008) Data quality assessment and the long-term trend of ground solar radiation in China. *J Appl Meteorol Clim* 47(4):1006–1016
- Su J, Huang J, Fu Q, Minnis P, Ge J, Bi J (2008) Estimation of Asian dust aerosol effect on cloud radiation forcing using Fu-Liou radiative model and CERES measurements. *Atmos Chem Phys* 8:2763–2771
- Tang JP, Wang PC, Xia X (2011) Modification of cloud screening method using ground-based broadband shortwave irradiance measurements. *Clim Environ Res* 16(5):609–619 (**In Chinese**)
- Waliser DE, Collins WD, Anderson SP (1996) An estimate of the surface shortwave cloud forcing over the western Pacific during TOGA COARE. *Geophys Res Lett* 23:519–522
- Wang K, Dickinson RE (2013) Global atmospheric downward long-wave radiation at the surface from ground-based observations, satellite retrievals, and reanalyses. *Rev Geophys* 51:150–185
- Wang M, Wei W, He Q, Yang Y, Fan L, Zhang J (2016) Summer atmospheric boundary layer structure in the hinterland of Taklimakan desert. *China J Arid Land* 8(6):846–860
- Wang M, Hu M, Huo W, Xu H, Li J, Li X (2017) Detecting sand-dust storms using a wind-profiling radar. *J Arid Land* 9(5):753–762
- Wild M (2009) Global dimming and brightening: a review. *J Geophys Res* 114:D00D16. <https://doi.org/10.1029/2008JD011470>
- Xiang H, Zhang F, Jiang J, Peng J, Zhang X, Zhang C (2014) Analysis of global cloud amount over the past 30 years based on CFSR data. *Meteorol Mon* 40(5):555–561 (**In Chinese**)
- Yang F, He Q, Huang J, Ali M, Yang X, Huo W, Zhou C, Liu X, Wei W, Cui C, Wang M, Li H, Yang L, Zhang H, Liu Y, Zheng X, Pan H, Jin L, Zou H, Zhou L, Liu Y, Zhang J, Meng L, Wang Y, Qin X, Yao Y, Liu H, Xue F, Zheng W (2021) Desert environment and climate observations network over the Taklimakan desert. *B AM Meteorol Soc*. <https://doi.org/10.1175/BAMS-D-20-0236>
- Zhang H, Peng J, Jing X, Li J (2013) The features of cloud overlapping in eastern Asia and their effect on cloud radiative forcing. *Sci China Earth Sci* 56(5):737–747
- Zhang H, Xie B, Liu Y, Wang F, Wang Z, Zhang J, Li J, Letu H, Shang H, Chen Y, Xuan Y (2017) Study on the influence of clouds on the Earth radiation budget and precipitation changes in East Asia region. *China Basic Sci* 5:18–22 (**In Chinese**)

Publisher's Note Springer Nature remains neutral with regard to jurisdictional claims in published maps and institutional affiliations.